ACS APPLIED MATERIALS & INTERFACES
Research Article
www.acsami.org

Bifunctional Manganese Ferrite/Polyaniline Hybrid as Electrode Material for Enhanced Energy Recovery in Microbial Fuel Cell

Santimoy Khilari,[†] Soumya Pandit,[‡] Jhansi L. Varanasi,[‡] Debabrata Das,[‡] and Debabrata Pradhan[*,†]

[†]Materials Science Centre and [‡]Department of Biotechnology, Indian Institute of Technology, Kharagpur 721302, West Bengal, India

Supporting Information

ABSTRACT: Microbial fuel cells (MFCs) are emerging as a sustainable technology for waste to energy conversion where electrode materials play a vital role on its performance. Platinum (Pt) is the most common material used as cathode catalyst in the MFCs. However, the high cost and low earth abundance associated with Pt prompt the researcher to explore inexpensive catalysts. The present study demonstrates a noble metal-free MFC using a manganese ferrite ($MnFe_2O_4$)/polyaniline (PANI)-based electrode material. The $MnFe_2O_4$ nanoparticles (NPs) and $MnFe_2O_4$ NPs/PANI hybrid composite not only exhibited superior oxygen reduction reaction (ORR) activity for the air cathode but also enhanced anode half-cell potential upon modifying carbon cloth anode in the single-chambered MFC. This is attributed to the improved extracellular electron transfer of exoelectrogens due to Fe^{3+} in $MnFe_2O_4$ and its capacitive nature. The present work demonstrates for the first time the dual property of $MnFe_2O_4$ NPs/PANI, i.e., as cathode catalyst and an anode modifier, thereby promising cost-effective MFCs for practical applications.

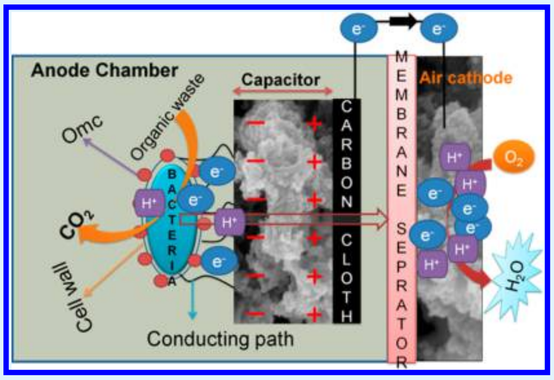

KEYWORDS: *spinel, oxygen reduction reaction catalyst, anode modifier, composites, green energy*

1. INTRODUCTION

Microbial fuel cell (MFC) has been one of the recent interests as a future alternative for energy production from wastes. It is based on the electrochemical catalytic reactions realized by exoelectrogenic bacteria (EB) adhered on the anode to produce electricity from biodegradable organic wastes.[1] The performance of any fuel cell strongly depends on the efficacy of the electrode.[2] Therefore, electrode design is a key factor for an efficient and inexpensive MFC fabrication. In recent years, efforts have been primarily directed toward synthesis of efficient electrode materials. In particular, the primary goals are to synthesize (i) a low cost anode to promote effective exoelectrogenic biofilm formation with high extracellular electron transfer (EET) and (ii) a catalyst with improved oxygen reduction reaction (ORR) kinetics at the cathode.[3] In all of the previous occasions, two different materials were applied in anode and cathode and their individual performance was evaluated.[4−6] In particular, oxide materials are employed as anode modifier and platinum (Pt) in the cathode.[4,5] The use of different materials in anode and cathode makes the process not only relatively complex but also expensive. Therefore, it is desirable to utilize a single bifunctional material which can meet the necessity of both electrodes for a viable MFC device.[7]

The cathodic ORR kinetics is considered as a major limiting factor for the power generation in a single-chambered MFC (sMFC).[6,8] Generally, sluggish ORR kinetics is improved by introducing Pt as electrocatalyst in the expense of its high cost and instability during long runs.[9] Thus, inexpensive metal oxides, metal complexes, heteroatom-doped carbon, and conducting polymer are considered alternatively to the Pt.[6,10−12] However, the performance of newly developed catalysts remains limited. So it is important to explore an efficient and economically viable ORR cathode catalyst.

Another important component of MFC is the anode which accepts electrons generated by EB during the oxidation process. The anodic electron transfer occurs via different EET mechanisms such as cell-surface proteins, excreted mediator compounds, and extracellular conductive pillis.[13] The slow EET process in the anode is one of the major limiting steps of MFC performance, which needs attention. The improvement of EET is mostly carried out by two approaches: (i) through isolation and genetic engineering of efficient EBs and (ii) using modified anode. The second approach is considered to be easier than the first one in terms of the complexity involved in the isolation of proper EB.[4,14,15] Generally, biocompatible conductive carbon paper/cloth, graphite, and stainless steel are utilized as anode in MFCs.[16] However, these materials lack electrochemical activity for the anode microbial reactions.[16] Therefore, it is imperative to develop suitable anode materials for efficient bacterial adhesion and electron collecting ability for the improved EET. Recently, nanostructured conducting polymers, TiO_2/graphene, SnO_2/MWCNTs, NiO, and RuO_2 modified anode have been developed to facilitate the anodic charge transfer process by reducing charge transfer resistance.[17−20] However,

Received: June 14, 2015
Accepted: August 28, 2015
Published: August 28, 2015

DOI: 10.1021/acsami.5b05273
ACS Appl. Mater. Interfaces 2015, 7, 20657−20666

the improvement is not significant to be practically used for the MFCs. Another engineering approach is to store the charge generated by EAB on an external capacitor and then discharge over a short period to power a device.[21] Thus, the implementation of an electrocapacitive material in the anode can accumulate the anodic charge like an internal capacitor, thus making the process simpler and more useful.[22] A few capacitive anodes based on Fe_3O_4, Fe_2O_3, and conducting polymer/RuO_2 composite have been developed in the recent past.[23−25] However, further improvement is necessary to increase the power generation ability of MFC. In addition, the outermost cytochrome's (Omc's) [i.e., Omc C and Omc A] electron transfer efficiency can be improved in the presence of the redox active biocompatible metal oxides and/or hydroxides.[26,27] Thus, redox active electrocapacitive metal oxides/hydroxides offer a platform for efficient EET with capacitive bioanode. Among the metal oxides, spinel type oxides offer a better choice because of the presence of different valent cations, high electrochemical capacitance, low cost, nontoxicity, high stability, and high electrical conductivity.[7,28] However, to date there are a very few reports on the single metal spinel oxides modified anode in MFC,[4] whereas there is no report on bimetallic spinel.

Manganese ferrite ($MnFe_2O_4$) is a spinel ferrite that exhibits electrocapacitive behavior with ORR catalytic activity as good as Pt.[28,29] However, the semiconducting nature of $MnFe_2O_4$ reduces its electrochemical activity.[28] Thus, the electrochemical activity of $MnFe_2O_4$ can be improved by incorporating it on a redox active conducting polymer such as polyaniline (PANI). PANI has been extensively used as catalyst support for several electrochemical applications including electrochemical energy storage devices such as supercapacitor due to its high conductivity, easy synthesis, high stability, and low cost.[30] Hence, the integration of $MnFe_2O_4$ and PANI could resolve the demerits that lie in the electrode materials, i.e., noncapacitive anode and poor ORR cathode catalyst.

In the present work, we report the synthesis of $MnFe_2O_4$/PANI composite and demonstrate it as an efficient bifunctional electrode material in the sMFCs for the first time. The performance of as-synthesized composite is compared with benchmark Pt/C ORR cathode catalyst. The anodic electron transfer efficiency and charge storage capacity of composite modified anode is also reported here, and its performance is compared with commonly used virgin carbon cloth (CC) anode. Furthermore, the PANI is demonstrated as a superior conducting catalyst support because of its improved performance over that of the conventional Vulcan XC carbon support. Vulcan XC carbon black is widely used as a support in the anode and cathode of fuel cells because of its high conductivity and easy dispersive nature.[8,12] The as-synthesized Pt-free bifunctional $MnFe_2O_4$/PANI composite is finally demonstrated as a superior electrode material in the sMFC for generating electricity from wastes.

2. MATERIALS AND METHODS

2.1. Chemicals. Aniline (99.9% (v/v)), hydrochloric acid (HCl, 35% (v/v)), ammonium persulfate [$(NH_4)_2S_2O_8$], ferric chloride ($FeCl_3$), manganese chloride tetra hydrate ($MnCl_2·4H_2O$), ammonia solution (25% (v/v)), and all other chemicals were purchased from Merck (Mumbai, India) and used without further purification. Pt/C was procured from Sigma-Aldrich, St. Louis, MO, USA and Vulcan XC was purchased from Cabot Corp., Mumbai, India.

2.2. Synthesis of $MnFe_2O_4$ Nanoparticles and PANI. $MnFe_2O_4$ nanoparticles ($MnFe_2O_4$ NPs) were synthesized by a simple hydrothermal route. In a typical synthesis 20 mL of 0.1 M $FeCl_3$ and 10 mL of 0.1 M $MnCl_2·4H_2O$ aqueous solution were mixed in a beaker and stirred at room temperature. Then 10 mL of 7.5% ammonia solution was added dropwise to the preceding mixture with vigorous stirring. The final mixture was transferred to a 50 mL Teflon-lined stainless steel autoclave and heated at 180 °C in a muffle furnace for 12 h. After completion of reaction, the furnace was allowed to cool naturally to room temperature. Then the precipitate formed inside the Teflon chamber was collected by centrifuging and washed with distilled water followed by ethanol for several times. Finally the product was dried at 60 °C in a vacuum oven.

PANI was synthesized by simple polymerization of aniline with $(NH_4)_2S_2O_8$ as oxidant. In a typical polymerization, 0.19 mL of pure aniline monomer was taken in 80 mL of ice cooled 1 M HCl solution. Then 20 mL of ice cooled 1 M HCl solution containing 570 mg of $(NH_4)_2S_2O_8$ was added and stirred for 12 h in an ice bath. Finally the green precipitate was collected by centrifuging and washed sequentially with 1 M HCl, distilled water, and ethanol. The washed precipitate was finally dried at 60 °C for 6 h in a vacuum oven.

2.3. Synthesis of $MnFe_2O_4$ NPs/PANI Composite. $MnFe_2O_4$ NPs/PANI composite was synthesized by incorporating $MnFe_2O_4$ NPs in PANI matrix during polymerization of aniline. In a typical synthesis, 120 mg of $MnFe_2O_4$ NPs was dispersed in 10 mL of 1 M HCl solution by bath sonication. In another beaker, 0.19 mL of pure aniline monomer was taken in 80 mL of ice cooled 1 M HCl solution. Subsequently 10 mL of 1 M HCl solution containing 570 mg of $(NH_4)_2S_2O_8$ was poured to the aniline solution with constant stirring. Then the $MnFe_2O_4$ NPs dispersion was added to this solution and stirred in an ice bath for 12 h. Finally the reaction product was collected, washed, and dried as described for PANI.

2.4. Synthesis of $MnFe_2O_4$ NPs/Vulcan XC Composite. $MnFe_2O_4$ NPs/Vulcan XC composite was synthesized by ultrasonically mixing $MnFe_2O_4$ NPs with Vulcan XC (60/40 (w/w)) in acetone and 10 wt % Nafion suspensions (Aldrich).

The details on catalyst characterization, membrane cathode assembly preparation, anode modification, bioelectrochemical measurements, and MFC operation are provided in the Supporting Information (SI).

3. RESULTS AND DISCUSSION

3.1. Morphology and Microstructures. The surface morphology and microstructures of the as-prepared samples were evaluated with field emission scanning electron microscope (FE-SEM) and transmission electron microscope (TEM), respectively. Parts a and b of Figure 1 show the FE-SEM and TEM images of near spherical $MnFe_2O_4$ NPs. The diameter of these NPs is measured to be in the range of 15−25 nm. Figure 1c shows the FESEM image of as-synthesized PANI revealing a fiber-like network structure. The diameter of these nanofibers is measured to be 50−100 nm. The TEM image of PANI nanofibers confirms their interpenetrating network structure (Figure 1d). Figure 1e shows an FESEM image of $MnFe_2O_4$ NPs/PANI composite. The $MnFe_2O_4$ NPs in the $MnFe_2O_4$ NPs/PANI composite appeared to be quite uniformly coated on the PANI nanofibers. The distribution of $MnFe_2O_4$ NPs on PANI nanofibers is evident in the TEM image as shown in Figure 1f. The diameter of $MnFe_2O_4$ NPs on PANI nanofibers is measured to be less than 30 nm as in the case of pristine $MnFe_2O_4$ NPs (Figure 1a,b).

The crystallographic phase and structure of as-synthesized $MnFe_2O_4$ NPs, PANI, and $MnFe_2O_4$ NPs/PANI composite were analyzed by powder X-ray diffraction (PXRD). The diffraction features in the PXRD pattern (Figure 2a) of $MnFe_2O_4$ NPs are indexed and assigned as per standard JCPDS File No. 0-074-2403 with cubic crystal structure. The calculated lattice constant of $MnFe_2O_4$ NPs was found to be a = 8.46 Å,

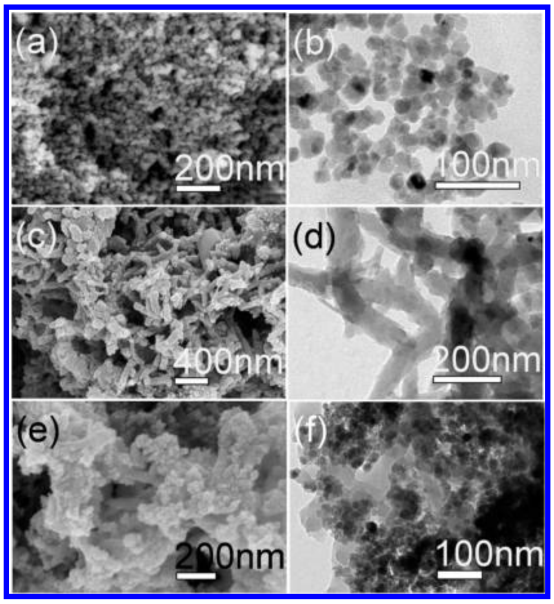

Figure 1. (a, c, e) FE-SEM and (b, d, f) TEM images of (a, b) MnFe$_2$O$_4$ NPs, (c, d) PANI, and (e, f) MnFe$_2$O$_4$ NPs/PANI composite.

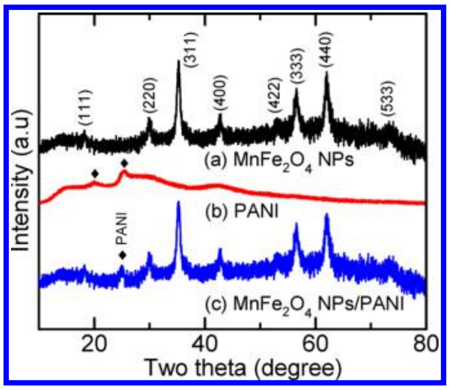

Figure 2. PXRD patterns of (a) MnFe$_2$O$_4$ NPs, (b) as-synthesized PANI, and (c) MnFe$_2$O$_4$ NPs/PANI composite.

which is close to the standard JCPDS value of a = 8.51 Å. The PXRD pattern of PANI (Figure 2b) shows two major peaks at 20.1° and 25.3° supporting the semicrystalline nature of PANI. These two peaks also indicate periodic arrangement of polymer chains in parallel and perpendicular directions.[31] The average interchain polymer separation was calculated using eq 1.[32]

$$R = 5/8[\lambda/\sin\theta] \tag{1}$$

where θ and λ represent the diffraction angle at the maximum intensity and the wavelength of incident X-ray, respectively. The interchain polymer separation of PANI is estimated to be 4.4 Å from the PXRD pattern shown as Figure 2b. The PXRD pattern of MnFe$_2$O$_4$ NPs/PANI composite is found to be similar to that of MnFe$_2$O$_4$ NPs as expected along with the major diffraction peak of PANI.

3.2. Electrochemical Study.

3.2.1. ORR Activity of MnFe$_2$O$_4$ NPs. The electrocatalytic activity of the as-synthesized catalysts (with a loading of 0.5 mg/cm^2 on the working electrode) toward ORR was evaluated by well-established electrochemical techniques such as cyclic voltammetry (CV), linear sweep voltammetry (LSV), and electrochemical impedance spectroscopy (EIS). The ORR performance of the as-synthesized MnFe$_2$O$_4$ NPs and MnFe$_2$O$_4$ NPs/PANI composite was compared with the MnFe$_2$O$_4$ NPs/Vulcan XC composite and benchmark Pt/C. The oxygen reduction was confirmed from the CVs recorded in O$_2$-saturated electrolyte with different catalysts that show distinct reduction peak at ∼− 0.1 V during cathodic sweep which is absent in N$_2$-saturated electrolyte (SI Figure S1). The reduction peak current is found to increase in the order of MnFe$_2$O$_4$ NPs < MnFe$_2$O$_4$ NPs/Vulcan XC composite < MnFe$_2$O$_4$ NPs/PANI composite, suggesting their ORR catalytic ability. Furthermore, the ORR peak is found to be shifted to less negative potential (from −0.109 to −0.080 V) indicating a decrease in overpotential for the reduction. This suggests that the ORR occurs at a faster rate with MnFe$_2$O$_4$ NPs/PANI composite than that of MnFe$_2$O$_4$ NPs and MnFe$_2$O$_4$ NPs/Vulcan XC composite. A more detail insight on ORR kinetics was obtained with LSV study using a rotating disk electrode (RDE) in 0.1 M pH 7 phosphate buffer solution (PBS). The steady state polarization plots as shown in Figure 3A were recorded at 1600 rpm with different catalysts. All of the LSV plots reveal three well-defined potential regions suggesting their ORR kinetics behavior: region I, kinetically controlled high potentials region (E > 0.1 V); region II, mixed diffusion-kinetic limited region (−0.3 to 0 V); and region III, diffusion limited region at lower potential (E < −0.3). The measured current density of MnFe$_2$O$_4$ NPs/PANI composite is higher than that of MnFe$_2$O$_4$ NPs and MnFe$_2$O$_4$ NPs/Vulcan XC composite and close to the benchmark Pt/C catalyst. In addition, the half-wave potential difference ($\Delta E_{1/2}$) is found to be very small (30 mV) between MnFe$_2$O$_4$ NPs/PANI and Pt/C indicating the former's ORR catalytic activity is comparable to the later. It is important to note that the polarization plot of MnFe$_2$O$_4$ NPs/PANI composite shows less negative onset potential and higher current density as compared to MnFe$_2$O$_4$ NPs/Vulcan XC composite, confirming PANI as better support material than that of Vulcan XC. Figure 3B shows the LSV plots with MnFe$_2$O$_4$ NPs/PANI composite electrode at different RDE

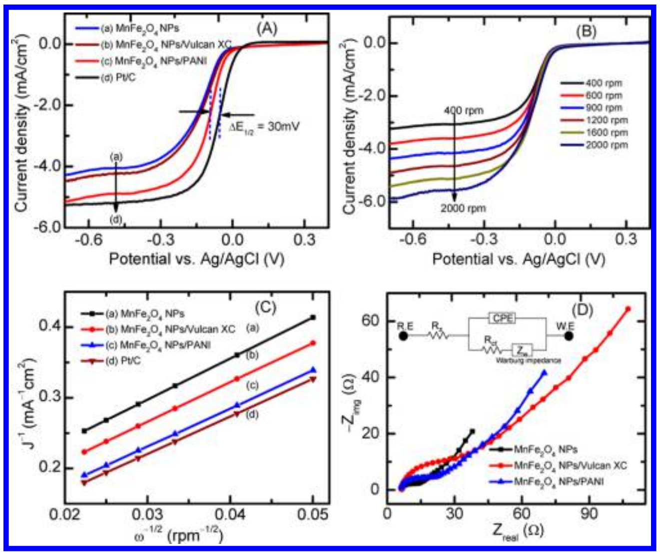

Figure 3. (A) Steady state polarization plots at 1600 rpm, (B) polarization plots of MnFe$_2$O$_4$ NPs/PANI composite recorded at different RDE rotation speeds, (C) Koutecky−Levich (K−L) plots of different catalysts, and (D) EIS spectra of different catalysts. The inset shows an equivalent circuit diagram.

rotation speeds. The increase in current density with RDE speed is similar to other ORR catalysts.[33] The ORR is known to follow two mechanisms on the catalyst surface. One is the efficient "four electron reduction path" and another is the less efficient "two electron reduction path". The detail on these two mechanisms is reported in our previous work.[8] In order to estimate the number of electron transfers involved in the present ORR process, Koutecky–Levich (K–L) equation (eq 2) is used.

$$1/J = 1/J_{\mathrm{L}} + 1/J_{\mathrm{K}} = 1/B\omega^{1/2} + 1/J_{\mathrm{K}} \tag{2}$$

where J, J_{L}, and J_{K} represent the measured current density, diffusion-limiting current density, and kinetic-limiting current density, respectively, at a RDE rotation speed "ω". B is determined from the slope of the K–L plots (Figure 3C) (J^{-1} vs $\omega^{-1/2}$) using the Levich equation (eq 3).

$$B = 0.2nFC_0(D_0)^{2/3}\upsilon^{-1/6} \tag{3}$$

where n is the number of electrons involved in the reaction, F is the Faraday constant (96485 C/mol), C_0 is the bulk oxygen concentration (1.26×10^{-3} mol/L), D_0 is the diffusion coefficient of oxygen in 0.1 M pH 7 PBS (2.7×10^{-5}cm^2/s), and υ is the kinematic viscosity of the electrolyte (0.01 cm^2/s).[33] The n values (considering n = 4 for Pt/C) for $MnFe_2O_4$ NPs and $MnFe_2O_4$ NPs/PANI composite were estimated to be 3.75 and 3.96, respectively. This indicates that $MnFe_2O_4$ NPs-based catalysts were ORR catalyzed via an efficient four electron path. It is important to note that the introduction of PANI significantly improves the ORR kinetics of $MnFe_2O_4$ NPs. This is attributed to the enhanced adsorption and reduction of O_2 molecules on the catalyst surface in the presence of π electron cloud of conducting PANI which facilitates the electron transport. The K–L plots (SI Figure S2) were also recorded at different potentials with $MnFe_2O_4$ NPs/PANI composite electrode in 0.1 M pH 7 PBS. The near parallel linear K–L plots at different potentials suggest identical electron transfer and first order reduction kinetics with respect to dissolved O_2. Thus, the synergy of redox active conducting support PANI and $MnFe_2O_4$ NPs made the present composite a promising electrocatalyst for ORR. The ORR catalytic activity in terms of n is comparable with the recently reported catalyst $MnCo_2O_4$/N-rmGO (n = 3.9) and cobalt oxide coupled nitrogen-doped graphene (n = 3.75).[34,35] Ma et al. reported n = 3.7 for iron oxide and partially graphitized carbon (Fe_3O_4/PGC–CS)-based ORR catalyst.[6] However, Zhu et al. reported 4.18 electron transfers per O_2 molecule for monodispersed $MnFe_2O_4$ nanoparticles.[29]

EIS has been extensively used to explore the electrode/electrolyte interfacial phenomenon. The charge transport and diffusion characteristics at an electrochemical interface are generally obtained from the complex impedance plot known as a Nyquist plot. Figure 3D shows the Nyquist plots with different catalysts displaying well-defined semicircle in the high frequency region along with a straight line in the low frequency region. The diameter of the semicircle arc suggests the charge transfer resistance (R_{ct}) of the respective electrode. All of the experimental data were fitted with an equivalent circuit consists of solution resistance (R_{s}), R_{ct}, constant phase element (CPE), and Warburg impedance (Z_{w}) (inset Figure 3D). A significant decrease in R_{ct} with $MnFe_2O_4$ NPs/PANI composite (12.1 Ω) was documented as compared to $MnFe_2O_4$ NPs/Vulcan XC composite (25.17 Ω) and $MnFe_2O_4$ NPs (33.12 Ω), indicating better charge transport property of the former. This improved activity is achieved due to well dispersion of $MnFe_2O_4$ NPs on conducting PANI matrix. Moreover the unique electronic structure of PANI provides active O_2 adsorption site on its surface which reduces the activation energy thereby improving charge transfer kinetic of ORR.

3.2.2. Specific Capacitance of $MnFe_2O_4$ NPs Composites.

The specific capacitance of as-synthesized $MnFe_2O_4$ NPs-based composites was measured to understand its role as anode modifier. The electrocapacitive behavior of $MnFe_2O_4$ NPs composite modified anode and virgin anode (i.e., unmodified CC) was evaluated by galvanostatic charge–discharge prior to the inoculation of anode chamber for MFC application. The specific capacitance of the anode was evaluated by using the following equation.[24]

$$C = \frac{I_{\mathrm{charge-discharge}}t}{U_{\mathrm{charge-discharge}}A} \tag{4}$$

where $I_{\mathrm{charge-discharge}}$ represents the charge–discharge current, t is the duration of discharge, $U_{\mathrm{charge-discharge}}$ refers to the potential window, and A is the projected area of anode. The electrochemical specific capacitance of bare CC was found to be 0.03 F/cm^2 (SI Figure S3). The specific capacitance increases to 0.6 F/cm^2 for $MnFe_2O_4$ NPs/Vulcan XC composite modified CC with a 0.25 mg/cm^2 loading of $MnFe_2O_4$ NPs/Vulcan XC (Figure 4). This signifies that $MnFe_2O_4$ NPs loaded Vulcan XC plays an active role on electrochemical charge storage on the electrode surface. In order to find optimum $MnFe_2O_4$ NPs/Vulcan XC loading, specific capacitance was measured with the different loadings. The ratio of $MnFe_2O_4$ NPs and Vulcan XC support was kept constant, i.e., 60:40 for all of the cases. The specific capacitance of $MnFe_2O_4$ NPs/Vulcan XC composite coated CC increases with loading as follows: 0.6 F/cm^2 (0.25 mg/cm^2) < 1.02 F/cm^2 (0.5 mg/cm^2) < 2.2 F/cm^2 (1 mg/cm^2) < 2.5 F/cm^2 (2 mg/cm^2). This suggests an insignificant improvement in specific capacitance with an increase in loading from 1 to 2 mg/cm^2. Similar experiments were performed with different loadings (0.25, 0.5, 1, and 2 mg/cm^2) of $MnFe_2O_4$ NPs/PANI. The increments of $MnFe_2O_4$ NPs/PANI content from 0.25 to 0.5 mg/cm^2 resulted in 87% improvement in specific capacitance and 2.18-fold increase in specific capacitance by doubling the loading from 0.5 to 1 mg/cm^2. However, further increase of

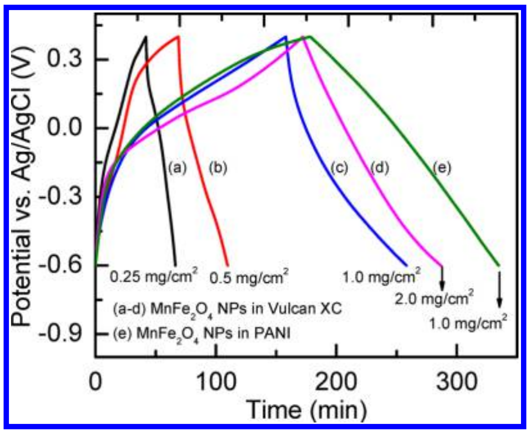

Figure 4. Galvanostatic charge–discharge profile of modified anodes with different loadings.

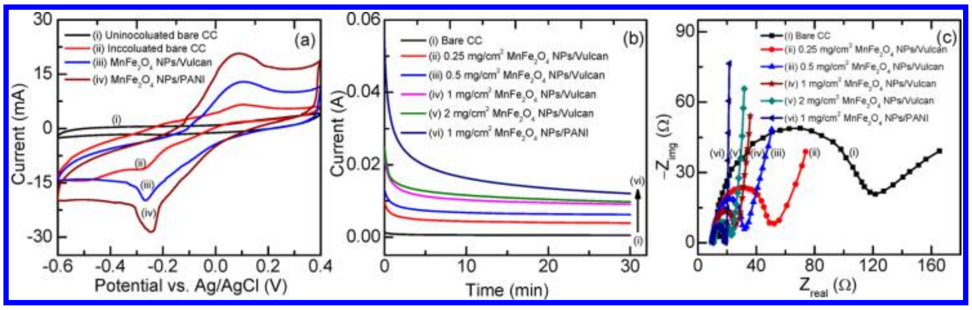

Figure 5. (a) Cyclic voltammogram, (b) chronoamperometric response (*i*–*t*) curves, and (c) Nyquist plots at OCP for different anodes.

$MnFe_2O_4$ NPs/PANI content (2 mg/cm^2) shows little improvement of specific capacitance (i.e., only 10% higher than 1 mg/cm^2 loading) as shown in Figure S4 (SI). This can be attributed to the formation of a thicker layer on the CC at higher loading and thus the capacitive material; i.e., $MnFe_2O_4$ NPs below the surface cannot be used for charge storage purpose. Thus, an optimum loading of 1 mg/cm^2 was taken for $MnFe_2O_4$ NPs/PANI composite coating the CC anode that delivers a capacitance of 3.8 F/cm^2, which is quite high as compared to $MnFe_2O_4$ NPs/Vulcan XC anode at the same loading. This higher capacitance is thus ascribed to better electrochemical properties of conducting PANI network.

3.2.3. Electrochemical Activity of Bioanodes. The electrochemical activity of different anodes was investigated with CV. The CVs show well-defined redox peaks both in anodic and cathodic sweeps which were absent in uninoculated electrolyte with bare CC as anode, indicating the catalytic activity of electroactive bacteria (EAB) (Figure 5a). All of the bioanodes have a characteristic reduction peak at ∼− 250 mV during the cathodic scan which signifies the reducing activity of *Shewanella putrefaciens* (*S. putrefaciens*) used as an EAB. This reduction peak is responsible for electron transfer from the electrochemically active heme group of Omc C to the electrode.[27,36] In the anodic scan, a broad oxidation peak was found at ∼0.09 V (vs Ag/AgCl), which indicates the oxidation of substrate and reduced species. The characteristic redox peaks are quite similar to other Shewanella species such as *S. oneidensis MR-1*, *S. putrefaciens MR-1*, *S. putrefaciens IR-1*, and *S. putrefaciens SR-21*.[27,36] The redox peak current was found to be increased with the $MnFe_2O_4$ modified bioanodes. The improvement of redox profile with modified bioanodes is believed to be due to the inherent electron transfer ability of *S. putrefaciens* from its Omc C to insoluble Fe(III) metal centers of $MnFe_2O_4$.[27,37] The enhanced electrochemical activity further suggests biocompatibility of the electrode modifier. It is also observed that the quasi-reversibility of electrodes increases, i.e., ΔE_p decreases, with the incorporation of $MnFe_2O_4$ NPs/PANI composite, which could be due to the availability of Fe(III) and Mn(II) sites and higher electrical and ionic conductivity of PANI. In the present case, PANI nanofibers with network structure act as nanowires for the improved EET by effective contact with redox active centers on bacterial Om.[38]

The charge storage efficiency of different capacitive anode modified electrode materials was studied from chronoamperograms recorded at open circuit potential (OCP) after stabilization of voltage in the MFC in the first three cycles. All of the chronoamperograms (Figure 5b) exhibit a high initial current that rapidly decreased to a steady value. This characteristic decay is quite similar to the previously reported study for polypyrrole/9,10-anthraquinone-2-sulfonic acid sodium salt composite anode modifier.[25] Further the profile depicts a higher current with an increase in capacitive $MnFe_2O_4$ material in the electrode, thus enhancing the charge storage activity. In addition, the magnitude of the current at the beginning of the discharge was highly dependent on the specific capacitance of the electrode material. The amount of charge released was evaluated from chronoamperogramms by using eq 5.

$$Q = \int_0^t I \, dt \tag{5}$$

where Q is the total charge accumulated, I is the discharge current, and t is the discharge time. It was found that the charge releasing property was dependent on the specific capacitance of the electrode material. By introducing 0.25 mg/cm^2 $MnFe_2O_4$ NPs/Vulcan XC composite (0.6 F/cm^2) on CC anode, ∼9.2 times improvement of charge storage capacity was obtained than that of bare CC. Furthermore, the $MnFe_2O_4$ NPs/PANI composite modified anode with 3.8 F/cm^2 specific capacitance delivers 2.48 C/cm^2 of charge which is 1.59 and 28.65 times higher than that of $MnFe_2O_4$ NPs/Vulcan XC composite (same loading) and bare CC anode, respectively. This confirms that the anode modified with high capacitance electrode modifier can function as a good biocapacitor by accumulating more electrons and then discharging them efficiently. Thus, the introduction of electrocapacitive $MnFe_2O_4$ NPs and PANI increase the charge storage capacity of the bioanodes. Under open circuit condition, electrons generated from substrate oxidation are temporarily stored in the reductive "extracytoplasmic cytochromes" of EABs.[39] However, in close circuit mode (with applied external resistance), the electrons stored in the outer cell membrane cytochromes are transferred to the anode surface.[40] A capacitive anode modifier can thus make a capacitive bridge between EAB and anode, which provide controlled flow of electrons generated by EAB to the anode. Thus, the higher the capacitance of the anode modifier the better is the performance. In the present study, the different valence metal centers of $MnFe_2O_4$ [Mn(II), Mn(IV), Fe(II), and Fe(III)] can serve as redox couple to interconnect the interface of EAB and the anode. Moreover, the continuous interconversion of Mn(II) to Mn(IV) and Fe(II) to Fe(III) is believed to contribute the transient storage of electrons via microbial or electrochemical reduction/oxidation resulting an increase in transient charge storage on $MnFe_2O_4$ loaded anodes. In addition, PANI is a redox active conducting polymer that provides a better platform for charge accumulation and transport in the $MnFe_2O_4$ NPs/PANI composite modified anode. This demonstrates the substantial increment of MFC performance with $MnFe_2O_4$ NPs/PANI composite as com-

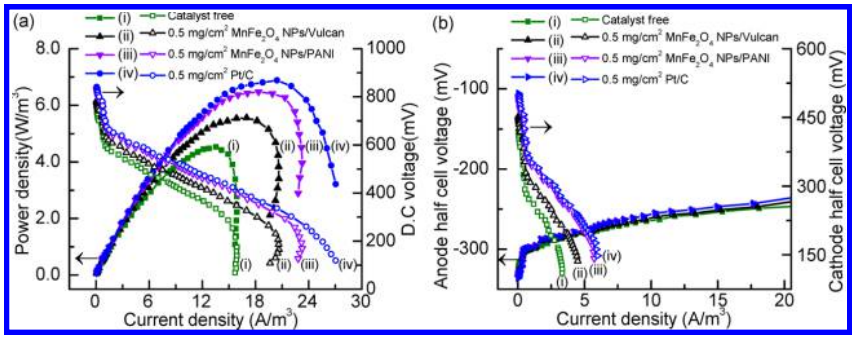

Figure 6. (a) Polarization plots for sMFC (power density and DC voltage as a function of current density) with different air cathodes. The power density and voltage data points are presented as solid and open symbols, respectively. (b) Anode and cathode polarization curves of sMFC with different catalysts supplemented to the cathode surface. Open and solid symbols represent cathode and anode half-cell voltages, respectively.

pared to MnFe$_2$O$_4$ NPs/Vulcan XC composite modified anode (discussed later).

The interfacial charge transfer activity of different bioanodes was studied by EIS analysis at OCP. The impedance characteristics of all electrodes are represented by Nyquist plots (Figure 5c). An equivalent circuit consists of R_s, R_{ct}, and Z_w, and CPE was used to evaluate the different resistive and capacitive characteristics of bioanodes. A significant decrease of R_{ct} was obtained by modifying bare CC (95.23 Ω) with MnFe$_2$O$_4$ NPs/Vulcan XC composite (35.59 Ω). Furthermore, R_{ct} decreased by increasing the loading of MnFe$_2$O$_4$ NPs/Vulcan XC composite on the CC, which indicates a better charge transfer ability of bioanodes with MnFe$_2$O$_4$ NPs/Vulcan XC composite. The multiple cation centers of redox active MnFe$_2$O$_4$ NPs is ascribed for better charge transfer and thus lower R_{ct}. However, very high loading of MnFe$_2$O$_4$ NPs leads to an increase in R_{ct} value due to formation of a thicker layer on the electrode surface and thus restricting easy movement of charge. Among all bioanodes, MnFe$_2$O$_4$ NPs/PANI modified anode exhibits the lowest R_{ct} value (11.21 Ω), suggesting PANI as a superior catalyst support to that of the conventional Vulcan XC. The CPE parameter also provides valuable information regarding capacitive characteristics of an electrode. It arises due to inhomogeneous electrode surface and nonuniform current distribution at the electrode. Generally CPE is defined by $Z_{CPE} = 1/c(j\omega)^y$, where c is the ideal capacitance and y ($0 \leq y \leq 1$) is an empirical constant. When $y = 1$, the electrode behaves like a real capacitor, and when $y = 0$, it reflects a complete resistor type electrode, whereas $y = 0.5$ indicates Warburg characteristics of the electrode. Thus, the y value close to unity signifies better electrocapacitive activity.[41,42] In the present study, bare CC anode showed $y = 0.43$, whereas MnFe$_2$O$_4$ NPs/PANI modified anode shows $y = 0.89$, close to unity. Other modified anodes have moderate y values in the range of 0.57−0.74 (Table S1, SI).

3.3. Effect of Bifunctional MnFe$_2$O$_4$ NPs Composites in the MFC Power Generation. The sMFC was fabricated using MnFe$_2$O$_4$ NPs composites as electrode material to study its performance for the power generation. The sMFCs were operated in batch cycle mode with cycle time of 60 ± 2 h. Initially, an anaerobic anodic chamber was fed with synthetic lactate wastewater without inoculation for 12 h. The pH of the wastewater was adjusted to 7.0 ± 0.1. Inoculation of the anodic chamber was carried out using a 10% (v/v) mid log phase culture of *S. putrefaciens* (2.9 g/L). After inoculation, anodic half-cell potential began decreasing owing to the donation of electrons to the anode by anodophile (EAB) and it reached at a plateau of about −289 ± 7 mV (vs Ag/AgCl) against an external resistance of 100 Ω for all of the MFCs. After three cycles, stabilized performance of the anodic half-cell was achieved and cathodic half-cell potential was measured with different composite loaded electrodes prepared in the present work.

3.3.1. Effect of MnFe$_2$O$_4$ NPs as ORR Catalyst. The effect of different ORR catalysts on the power generation in sMFC was studied using a bare CC cloth as anode in all of the cases. Figure S5 (SI) shows the current production curves for different sMFCs to indicate the initial increment of current and followed by stabilization after six cycles with the composite catalyst and Pt/C. The present current production profile is similar to the previous report.[43] The initial and stabilized current production was found to follow the order of catalyst-free < MnFe$_2$O$_4$ NPs/Vulcan XC < MnFe$_2$O$_4$ NPs/PANI < Pt/C as cathode. The catalyst-free MFC has the cathode with only Vulcan XC (without MnFe$_2$O$_4$ NPs). The sMFC cathode with only Vulcan XC, i.e., catalyst-free, produced a maximum volumetric power density ($P_{d,max}$) of 4.45 W/m^3 [Figure 6a(i)], which increases to 5.55 W/m^3 [Figure 6a(ii) and Table S2, SI] by introducing 0.5 mg/cm^2 MnFe$_2$O$_4$ NPs/Vulcan XC onto the cathode surface. By replacing Vulcan XC with PANI, a substantial enhancement (more than 1.45-fold compared to catalyst-free cathode) of the $P_{d,max}$ (6.49 W/m^3) is achieved [Figure 6a(iii)]. It is important to note that the $P_{d,max}$ of MnFe$_2$O$_4$ NPs/PANI loaded (0.5 mg/cm^2) cathode is only 6% less than that of the same loading of benchmark Pt/C cathode (6.88 W/m^3) [Figure 6a(iv)]. The maximum OCP, columbic efficiency (C_E), and chemical oxygen demand (COD) removal efficiency were measured and found to be increased whereas the internal resistance is decreased from the catalyst-free cathode to MnFe$_2$O$_4$ NPs/PANI loaded cathode (Table S2, SI). It concludes that MnFe$_2$O$_4$ NPs and PANI synergistically improved the ORR activity at the cathode, resulting in enhanced current production and power output. The reduction of internal resistance with PANI signifies better electrode kinetics due to lower charge transfer resistance in accord with EIS study (Figure 5c). The half-cell potential measurements reveal that all sMFCs with bare CC anode have similar half-cell potentials at the same current (Figure 6b, curve with solid symbol). Thus, the differences in power production from these four sMFC reactors resulted from the differences in the cathode potentials (Figure 6b, curve with open symbol).

3.3.2. Effect of MnFe$_2$O$_4$ NPs Composites Anode Modifier. To find the influence of MnFe$_2$O$_4$ NPs as anode modifier, four different loadings of MnFe$_2$O$_4$ NPs/Vulcan XC, i.e., 0.25 mg/

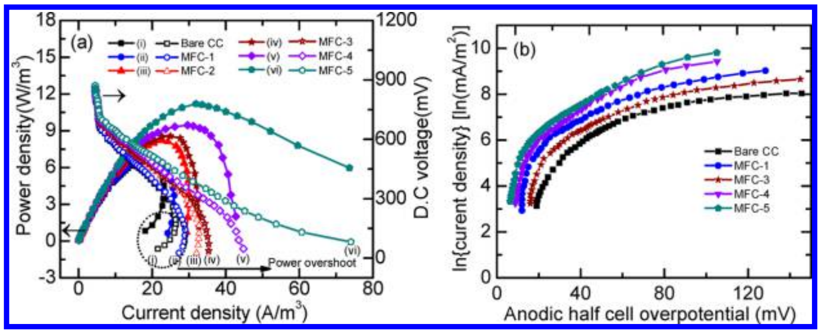

Figure 7. (a) Polarization plots for sMFC (power density and DC voltage as a function of current density) with different anodes. The power density and voltage data points are presented as solid and open symbols, respectively. (b) Tafel plots of different modified anodes.

cm^2 (MFC-1), 0.5 mg/cm^2 (MFC-2), 1.0 mg/cm^2 (MFC-3), and 2 mg/cm^2 (MFC-4) (Table S3, SI), were considered, keeping the catalyst loading (0.5 mg/cm^2 $MnFe_2O_4$ NPs/PANI) in the cathode constant. In addition, the 1 mg/cm^2 $MnFe_2O_4$ NPs/PANI composite incorporated anode was studied and termed as MFC-5. The ratio of anode modifier, i.e., $MnFe_2O_4$ NPs, and the support, i.e., Vulcan XC or PANI, was kept at constant ratio of 60:40 for all of the cases. Stabilized voltage was obtained in these MFCs after three cycles (i.e., 7 days of operation) of post inoculation. The current generation in all of the MFCs gradually increased with time and stabilized after nine cycles of operation (i.e., after 21 days, 1 cycle = 60 ± 2 h) as shown in Figure S6 (SI). In addition, the stabilized current production is found to increase with increasing $MnFe_2O_4$ NPs/Vulcan XC loading in the anode. This suggests the requirement of capacitive anode modifier for the charge accumulation which in turn produces higher current. Upon replacing Vulcan XC with PANI (MFC-5), a considerable increment of current production suggests PANI as a better conducting support than that of Vulcan XC. After nine cycles, the voltage output of MFC-4 sharply increased and stabilized at about −298 ± 4 mV on day 21 (not shown). A slightly lower voltage of −286 ± 3 mV was obtained in MFC-3. MFC-1 and MFC-2 show a slower increase in current in these cycles. Moreover, a significant increase in anodic half-cell potential (−301 ± 3 mV) was recorded with MFC-5 (1 mg/cm^2 $MnFe_2O_4$ NPs/PANI) after 21 days, suggesting PANI as the most suitable support material along with $MnFe_2O_4$ NPs as anode modifier. Polarization curves as shown in Figure 7a were obtained using an adjustable external resistance after the MFCs reached the steady maxima in their OCP. The resistors were used both in increasing and decreasing order of the resistance. However, the voltage profile showed hysteresis; i.e., the polarization curves did not overlap in both directions (not shown), and the reason for which is not well understood. All of the polarization results shown in this work were recorded when the resistors switched from higher to lower external resistance. The stabilized voltage was noted after 15 min of external resistance loading. The corresponding polarization curves of different MFCs, as shown in Figure 7a, were obtained by varying the external resistance from 90 kΩ to10 Ω. The maximum OCP and operating current in MFC-4 was measured to be 0.871 V and 3.27 mA, respectively. The maximum sustainable volumetric power density (at 100 Ω) of 9.45 W/m^3 (normalized to the working volume of the anode chamber) was obtained for MFC-4, which decreases to 8.56 W/m^3 (MFC-3), 8.2 W/m^3 (MFC-2), and 6.77 W/m^3 (MFC-1) as presented in Table S3 (SI). It is important to note that, at high current regime (30−10 Ω R_{ext}), significant power overshoot (rapid drop of current and voltage) occurred in sMFCs with bare CC anode or catalyst free [Figure 7a(i)] and anode containing smaller quantity of modifier [MFC-1, 0.25 mg/cm^2]. The power overshoot is normally observed in the high current density region when both the cell voltage and current rapidly decrease due to an increase in the internal resistance of MFC.[44] In order to find out the exact reason for the power overshoot, the individual electrode potentials were measured ,and the results obtained from the half-cell experiments indicate that it is related to the electrochemical activity of the anode biofilm.[45] The earlier reports suggest that, under open circuit MFC operation, the bioflim behaves like an electrochemical capacitor. The electrons generated owing to enzymatic oxidation of the substrate are temporarily stored in the cyctrochromes and/or self-produced mediators of EB contributing a capacitor characteristic to the bioflim.[46] These stored electrons are subsequently released to the electrode by applying an external load (close circuit operation) and producing a current on the external circuit. A low capacitance of biofilm makes the system unstable at high current density regime (low external resistance) of polarization study where the discharge rate of anodic charge is very high.[46] In this context, application of an additional abiotic capacitive material on the anode can retain stability of MFC at high current regime. In the present study, the power overshoot was found to be prominent with bare CC indicating insufficient biocapacitance of anodic bioflim. Incorporation of 0.25 mg/cm^2 $MnFe_2O_4$ NPs/Vulcan XC was found to be not enough to eliminate the power overshoot, but at a loading of 0.5 mg/cm^2 the power overshoot did not occurred. Thus, a larger amount of capacitive $MnFe_2O_4$ NPs/Vulcan XC improves the transient charge storage at the anode surface as was also supported from chronoamperometry study of bioanodes [Figure 5b]. This implies the requirement of higher anodic capacitance to prevent the power overshoot. It is also to be noted that the presence of active metal centers [Fe(II), Fe(III), Mn(II), and Mn(IV)] in $MnFe_2O_4$ NPs can contribute pseudocapacitance and dramatically improves anodic capacitance.[47] An increase in the anodic capacitance due to the presence of pseudocapacitive modifiers not only eliminates the power overshoot but also improves power production.[48] Furthermore, MFC-5 produced the highest maximum volumetric power density of 11.2 W/m^3 and operating current of 3.51 mA (at R_{ext} = 100 Ω) indicating the superiority of PANI over Vulcan XC support. To find the exact role and contribution of PANI, a controlled experiment was performed with 0.5 and 1.0 mg/cm^2 PANI loadings on cathode and anode, respectively. No cathode catalyst and anode modifiers

($MnFe_2O_4$ NPs) are used in this controlled experiment, which is termed as MFC-C (Table S3, SI). The polarization plot for MFC-C is shown in Figure S7 (SI). The maximum power density of 6.1 W/m^3 and 811 mV OCP were documented with MFC-C, which are lower than that of any MFC incorporated with $MnFe_2O_4$ NPs (Table S3, SI). This clarifies that although PANI is a superior support material to that of Vulcan XC, $MnFe_2O_4$ NPs contributes majorly to the improved power generation from sMFC. The improved power generation with $MnFe_2O_4$ NPs modified anode can also be ascribed to a large population of bacteria that colonize in the presence of $MnFe_2O_4$ NPs. Consequently, large negative potential developed owing to more electron donation by EAB at the anode even at low external resistance. The SEM image (Figure S8, SI) of bioanode confirms considerable accumulation of EAB on the anode surface with $MnFe_2O_4$ NPs. Furthermore, the electrocapacitive behavior of $MnFe_2O_4$ NPs modified anode offers control discharge around all external resistance. It is to be noted that the cell potential here is mainly governed by anode potential. All of the MFCs (MFC-1 to MFC-5 and bare CC anode MFC) deliver the same cathode half-cell potential. However, the anode potentials were different. The anode potential (oxidation) can be correlated with the metabolic activities of electrogenic microorganism. The power density obtained with $MnFe_2O_4$ NPs/PANI (1 mg/cm^2 loading) is compared with several recently reported metal oxide and/or PANI modified anodes. The power density obtained in the present work is close to the reported study where Pt and/or potassium ferricyanide are used in the MFCs (Table S4).[5,17,20,49,50] It must be noted that there is no previous report on the MFC where both anode and cathode are modified with non-noble catalyst and/or modifier.

To understand the change in anodic half-cell potential, a Tafel test (Figure 7b) was carried out with unmodified and modified bioanodes. The electron transfer from anode to the cathode is generally hampered by different losses which lower the power conversion efficiency of the MFCs. The electrons generated from the substrate degradation need to overcome various barriers to transfer from the biocatalyst to the anode and then to the cathode prior to getting reduced at the cathode, which incurs energy loss and can account for underactivation losses. The voltage drop due to activation losses in MFCs can be expressed by a semiempirical Tafel equation (eq 6), where ΔV is the overpotential, A = Tafel constant (the higher the A value, the lower is the electrode kinetics), and i_o = the exchange current density (cell current normalized to the anode surface area).

$$\Delta V = A \ln\left(\frac{i}{i_o}\right) \tag{6}$$

MFC equipped with bare CC anode shows the lowest exchange current density (0.007 mA/m^2) and highest Tafel constant (238 mV). However, the modified anodes show improvement in the exchange current density and reduction of the Tafel constant in the order of MFC-1 (0.028 mA/m^2, 143 mV) < MFC-3 (0.037 mA/m^2, 109 mV) < MFC-4 (0.052 mA/m^2, 51 mV) < MFC-5 (0.074 mA/m^2, 17 mV) measured from Figure 7b. This indicates the improvement in the bioelectrochemical activity due to reduction in the activation losses with $MnFe_2O_4$ NPs modified anode. It is important to note that iron-reducing microbes, including *S. putrefaciens*, *Desulfuromonas acetoxidans*, and *Geobacter metallireducens*, can conserve energy by coupling the oxidation of organic compounds to the reduction of Fe^{3+}. Myers et al. suggested that *S. putrefaciens* coupled the anaerobic reduction of Fe^{3+} or Mn^{4+} to respiration-linked proton translocation. It was also reported by Myers et al. that when *S. putrefaciens* is grown anaerobically, 80% of its cytochromes are localized in the outer membrane.[51] In the anode chamber of MFC, bioreduction of the anode may involve direct reduction by c-type cytochromes located in the outer membrane of these EABs, such as Shewanella, which possess 42 c-type cytochromes (c-Cyts) in various positions at the inner and outer membranes. These cytochromes act as a "molecular wire" and play an important role in the electron transfer process. Shewanella has the affinity toward the Fe(III) and Mn(IV) oxides and thus can initiate EET to the attached iron oxides as a terminal process in its metabolism.[52] In the present study, $MnFe_2O_4$ with different valence metal centers [Fe(II), Fe(III), Mn(II), and Mn(IV)] shows promising activity for improved EET resulting in improved power generation in the sMFC.

4. CONCLUSIONS

The present study demonstrates $MnFe_2O_4$ spinel as a novel bifunctional catalyst in the sMFC. Incorporation of $MnFe_2O_4$ NPs on Vulcan XC or PANI significantly improves catalytic activity of both the anode and cathode. In particular, the ORR activity of $MnFe_2O_4$ NPs/PANI composite is found to be comparable to the standard Pt/C in cathode. The anode half-cell potential is measured to be larger for the anode modified with $MnFe_2O_4$ NPs and thereby generating more power in the sMFC as compared to bare CC. The power overshoot problem is also substantially reduced by increasing the $MnFe_2O_4$ NPs composite loading in the anode. The significant improvement of anode performance in sMFC is attributed to the multivalence cations and capacitive behavior of $MnFe_2O_4$ NPs as demonstrated in the present work. Furthermore, electrochemically active PANI is demonstrated as a better catalyst support as compared to conventional Vulcan XC. The present noble metal-free sMFC with a bifunctional spinel catalyst is promising for the inexpensive green energy generation systems.

■ ASSOCIATED CONTENT

Ⓢ Supporting Information

This material is available free of charge via the Internet The Supporting Information is available free of charge on the ACS Publications website at DOI: 10.1021/acsami.5b05273.

> Detail characterization of catalysts, membrane cathode assembly fabrication, cyclic voltammograms, Koutecky–Levich (K–L) plots, galvanostatic charge–discharge profile, electrochemical impedance characteristics, current production profile of catalyst modified cathode and anode, sMFC performance, and SEM images of bioanodes (PDF)

■ AUTHOR INFORMATION

Corresponding Author

*E-mail: deb@matsc.iitkgp.ernet.in.

Notes

The authors declare no competing financial interest.

■ ACKNOWLEDGMENTS

S.K. acknowledges the fellowship from the University Grant Commission (UGC), New Delhi. This work is supported by the Council of Scientific & Industrial Research [Grant No. 01(2724)/13/EMR-II], New Delhi, India.

■ REFERENCES

(1) Liu, J.; Yong, Y.-C.; Song, H.; Li, C. M. Activation Enhancement of Citric Acid Cycle to Promote Bioelectrocatalytic Activity of *arcA* Knockout *Escherichia coli* Toward High-Performance Microbial Fuel Cell. *ACS Catal.* **2012**, *2*, 1749−1752.

(2) Liew, K. B.; Daud, W. R. W.; Ghasemi, M.; Leong, J. X.; Lim, S. S.; Ismail, M. Non-Pt Catalyst as Oxygen Reduction Reaction in microbial fuel cells: A Review. *Int. J. Hydrogen Energy* **2014**, *39*, 4870−4883.

(3) Zhou, M.; Chi, M.; Luo, J.; He, H.; Jin, T. An Overview of Electrode Materials in Microbial Fuel Cells. *J. Power Sources* **2011**, *196*, 4427−4435.

(4) Peng, X.; Yu, H.; Wang, X.; Zhou, Q.; Zhang, S.; Geng, L.; Sun, J.; Cai, Z. Enhanced Performance and Capacitance Behavior of Anode by Rolling Fe_3O_4 into Activated Carbon in Microbial Fuel Cells. *Bioresour. Technol.* **2012**, *121*, 450−453.

(5) Wang, Y.; Li, B.; Zeng, L.; Cui, D.; Xiang, X.; Li, W. Polyaniline/mesoporous Tungsten Trioxide Composite as Anode Electrocatalyst for High-Performance Microbial Fuel Cells. *Biosens. Bioelectron.* **2013**, *41*, 582−588.

(6) Ma, M.; Dai, Y.; Zou, J.; Wang, L.; Pan, K.; Fu, H. Synthesis of Iron Oxide/Partly Graphitized Carbon Composites as a High-Efficiency and Low-Cost Cathode Catalyst for Microbial Fuel Cells. *ACS Appl. Mater. Interfaces* **2014**, *6*, 13438−13447.

(7) Manivasakan, P.; Ramasamy, P.; Kim, J. Use of Urchin-like $Ni_xCo_{3-x}O_4$ Hierarchical Nanostructures Based on Non-Precious Metals as Bifunctional Electrocatalysts for Anion-Exchange Membrane Alkaline Alcohol Fuel Cells. *Nanoscale* **2014**, *6*, 9665−9672.

(8) Khilari, S.; Pandit, S.; Ghangrekar, M. M.; Das, D.; Pradhan, D. Graphene Supported α-MnO_2 Nanotubes as a Cathode Catalyst for Improved Power Generation and Wastewater Treatment in Single-Chambered Microbial Fuel Cells. *RSC Adv.* **2013**, *3*, 7902−7911.

(9) Xie, X.; Pasta, M.; Hu, L.; Yang, Y.; McDonough, J.; Cha, J.; Criddle, C. S.; Cui, Y. Nano-Structured Textiles as High-Performance Aqueous Cathodes for Microbial Fuel Cells. *Energy Environ. Sci.* **2011**, *4*, 1293−1297.

(10) Liu, Y.; Liu, H.; Wang, C.; Hou, S.-X.; Yang, N. Sustainable Energy Recovery in Wastewater Treatment by Microbial Fuel Cells: Stable Power Generation with Nitrogen-doped Graphene Cathode. *Environ. Sci. Technol.* **2013**, *47*, 13889−13895.

(11) Xia, X.; Zhang, F.; Zhang, X.; Liang, P.; Huang, X.; Logan, B. E. Use of Pyrolyzed Iron Ethylenediaminetetraacetic Acid Modified Activated Carbon as Air−Cathode Catalyst in Microbial Fuel Cells. *ACS Appl. Mater. Interfaces* **2013**, *5*, 7862−7866.

(12) Ahmed, J.; Kim, H. J.; Kim, S. Polyaniline Nanofiber/Carbon Black Composite as Oxygen Reduction Catalyst for Air Cathode Microbial Fuel Cells. *J. Electrochem. Soc.* **2012**, *159*, B497−B501.

(13) Peng, L.; You, S.-J.; Wang, J.-Y. Carbon Nanotubes as Electrode Modifier Promoting Direct Electron Transfer from *Shewanella oneidensis*. *Biosens. Bioelectron.* **2010**, *25*, 1248−1251.

(14) Dávila, D.; Esquivel, J. P.; Vigués, N.; Sánchez, O.; Garrido, L.; Tomás, N.; Sabaté, N.; del Campo, F. J.; Muñoz, F. J.; Mas, J. Development and Optimization of Microbial Fuel cells. *J. New Mater. Electrochem. Syst.* **2008**, *11*, 99−103.

(15) Rabaey, K. *Bioelectrochemical Systems: From Extracellular Electron Transfer to Biotechnological Application*; IWA: London, NY, USA, 2010; pp 101−113.

(16) Wei, J.; Liang, P.; Huang, X. Recent Progress in Electrodes for Microbial Fuel Cells. *Bioresour. Technol.* **2011**, *102*, 9335−9344.

(17) Zhao, C.; Wang, W.-J.; Sun, D.; Wang, X.; Zhang, J.-R.; Zhu, J.-J. Nanostructured Graphene/TiO_2 Hybrids as High-Performance Anodes for Microbial Fuel Cells. *Chem. - Eur. J.* **2014**, *20*, 7091−7097.

(18) Mehdinia, A.; Ziaei, E.; Jabbari, A. Multi-Walled Carbon nanotube/SnO_2 Nanocomposite: A Novel Anode Material for Microbial Fuel Cells. *Electrochim. Acta* **2014**, *130*, 512−518.

(19) Lv, Z.; Xie, D.; Yue, X.; Feng, C.; Wei, C. Ruthenium Oxide-Coated Carbon Felt Electrode: A Highly Active Anode for Microbial Fuel Cell Applications. *J. Power Sources* **2012**, *210*, 26−31.

(20) Qiao, Y.; Wu, X.-S.; Li, C. M. Interfacial Electron Transfer of *Shewanella putrefaciens* Enhanced by Nanoflaky Nickel Oxide Array in Microbial Fuel Cells. *J. Power Sources* **2014**, *266*, 226−231.

(21) Dewan, A.; Beyenal, H.; Lewandowski, Z. Intermittent Energy Harvesting Improves the Performance of Microbial Fuel Cells. *Environ. Sci. Technol.* **2009**, *43*, 4600−4605.

(22) Deeke, A.; Sleutels, T. H. J. A.; Hamelers, H. V. M; Buisman, C. J. N. Capacitive Bioanodes Enable Renewable Energy Storage in Microbial Fuel Cells. *Environ. Sci. Technol.* **2012**, *46*, 3554−3560.

(23) Peng, X.; Yu, H.; Ai, L.; Li, N.; Wang, X. Time Behavior and Capacitance Analysis of Nano-Fe_3O_4 Added Microbial Fuel Cells. *Bioresour. Technol.* **2013**, *144*, 689−692.

(24) Pandit, S.; Khilari, S.; Roy, S.; Pradhan, D.; Das, D. Improvement of Power Generation Using *Shewanella putrefaciens* Mediated Bioanode in a Single Chambered Microbial Fuel Cell: Effect of Different Anodic Operating Conditions. *Bioresour. Technol.* **2014**, *166*, 451−457.

(25) Lv, Z.; Xie, D.; Li, F.; Hu, Y.; Wei, C.; Feng, C. Microbial Fuel Cell as a Biocapacitor by Using Pseudo-Capacitive Anode Materials. *J. Power Sources* **2014**, *246*, 642−649.

(26) Peng, X.; Yu, H.; Wang, X.; Gao, N.; Geng, L.; Ai, L. Enhanced Anode Performance of Microbial Fuel Cells by Adding Nano-semiconductor Goethite. *J. Power Sources* **2013**, *223*, 94−99.

(27) Deng, L.; Guo, S.; Liu, Z.; Zhou, M.; Li, D.; Liu, L.; Li, G.; Wang, E.; Dong, S. To Boost c-Type Cytochrome Wire Efficiency of Electrogenic Bacteria with Fe_3O_4/Au Nanocomposites. *Chem. Commun.* **2010**, *46*, 7172−7174.

(28) Sankar, K. V.; Selvan, R. K. The Preparation of $MnFe_2O_4$ Decorated Flexible Graphene Wrapped with PANI and Its Electrochemical Performances for Hybrid Supercapacitors. *RSC Adv.* **2014**, *4*, 17555−17566.

(29) Zhu, H.; Zhang, S.; Huang, Y.-X.; Wu, L.; Sun, S. Monodisperse M_x Fe_{3-x} O_4 (M = Fe, Cu, Co, Mn) Nanoparticles and Their Electrocatalysis for Oxygen Reduction Reaction. *Nano Lett.* **2013**, *13*, 2947−2951.

(30) Wang, L.; Lu, X.; Lei, S.; Song, Y. Graphene-Based Polyaniline Nanocomposites: Preparation, Properties and Applications. *J. Mater. Chem. A* **2014**, *2*, 4491−4509.

(31) Xu, F.; Zheng, G.; Wu, D.; Liang, Y.; Li, Z.; Fu, R. Improving Electrochemical Performance of Polyaniline by Introducing Carbon Aerogel as Filler. *Phys. Chem. Chem. Phys.* **2010**, *12*, 3270−3275.

(32) Khilari, S.; Pandit, S.; Das, D.; Pradhan, D. Manganese Cobaltite/polypyrrole Nanocomposite-Based Air-Cathode for Sustainable Power Generation in the Single-Chambered Microbial Fuel Cells. *Biosens. Bioelectron.* **2014**, *54*, 534−540.

(33) Su, Y.; Zhu, Y.; Yang, X.; Shen, J.; Lu, J.; Zhang, X.; Chen, J.; Li, C. A Highly Efficient Catalyst toward Oxygen Reduction Reaction in Neutral Media for Microbial Fuel Cells. *Ind. Eng. Chem. Res.* **2013**, *52*, 6076−6082.

(34) Liang, Y.; Wang, H.; Zhou, J.; Li, Y.; Wang, J.; Regier, T.; Dai, H. Covalent Hybrid of Spinel Manganese−Cobalt Oxide and Graphene as Advanced Oxygen Reduction Electrocatalysts. *J. Am. Chem. Soc.* **2012**, *134*, 3517−3523.

(35) He, Q.; Li, Q.; Khene, S.; Ren, X.; López-Suárez, F. E.; Lozano-Castelló, D.; Bueno-López, A.; Wu, G. High-Loading Cobalt Oxide Coupled with Nitrogen-Doped Graphene for Oxygen Reduction in Anion-Exchange-Membrane Alkaline Fuel Cells. *J. Phys. Chem. C* **2013**, *117*, 8697−8707.

(36) Kim, H. J.; Park, H. S.; Hyun, M. S.; Chang, I. S.; Kim, M.; Kim, B. H. A Mediator-Less Microbial Fuel Cell Using a Metal Reducing Bacterium. *Enzyme Microb. Technol.* **2002**, *30*, 145−152.

(37) Lovley, D. R. Extracellular Electron Transfer: Wires, Capacitors, Iron Lungs, and More. *Geobiology* **2008**, *6*, 225−231.

(38) Zhao, Y.; Watanabe, K.; Nakamura, R.; Mori, S.; Liu, H.; Ishii, K.; Hashimoto, K. Three-Dimensional Conductive Nanowire Net-

works for Maximizing Anode Performance in Microbial Fuel Cells. *Chem. - Eur. J.* **2010**, *16*, 4982−4985.

(39) Stams, A. J. M.; de Bok, F. A. M.; Plugge, C. M.; van Eekert, M. H. A.; Dolfing, J.; Schraa, G. Electron Transfer in Anaerobic Microbial Communities. *Environ. Microbiol.* **2006**, *8*, 371−382.

(40) Chang, I. S.; Moon, H.; Bretschger, O.; Jang, J. K.; Park, H. I.; Nealson, K. H.; Kim, B. H. Electrochemically Active Bacteria (EAB) and Mediator-Less Microbial Fuel Cells. *J. Microbiol. Biotechnol.* **2006**, *16*, 163−177.

(41) Barsoukov, E., Macdonald, J. R., Eds.; *Impedance Spectroscopy: Theory, Experiment, and Applications*, 2nd ed.; Wiley-Interscience: Hoboken, NJ, USA, 2005; p 87.

(42) Sidhu, N.; Rastogi, A. C. Vertically Aligned ZnO Nanorod Core-Polypyrrole Conducting Polymer Sheath and Nanotube Arrays for Electrochemical Supercapacitor Energy Storage. *Nanoscale Res. Lett.* **2014**, *9*, 453−468.

(43) Zhao, C.; Wu, J.; Kjelleberg, S.; Loo, J. S. C.; Zhang, Q. Employing a Flexible and Low-Cost Polypyrrole Nanotube Membrane as an Anode to Enhance Current Generation in Microbial Fuel Cells. *Small* **2015**, *11*, 3440−3443.

(44) Winfield, J.; Ieropoulos, I.; Greenman, J.; Dennis, J. The overshoot phenomenon as a function of internal resistance in microbial fuel cells. *Bioelectrochemistry* **2011**, *81*, 22−27.

(45) Hong, Y.; Call, D. F.; Werner, C. M.; Logan, B. E. Adaptation to high current using low external resistances eliminates power overshoot in microbial fuel cells. *Biosens. Bioelectron.* **2011**, *28*, 71−76.

(46) Peng, X.; Yu, H.; Yu, H.; Wang, X. Lack of anodic capacitance causes power overshoot in microbial fuel cells. *Bioresour. Technol.* **2013**, *138*, 353−358.

(47) Kuo, S.-L.; Lee, J.-F.; Wu, N.-L. Study on Pseudocapacitance Mechanism of Aqueous $MnFe_2O_4$ Supercapacitor. *J. Electrochem. Soc.* **2007**, *154*, A34−A38.

(48) Feng, C.; Lv, Z.; Yang, X.; Wei, C. Anode modification with capacitive materials for a microbial fuel cell: an increase in transient power or stationary power. *Phys. Chem. Chem. Phys.* **2014**, *16*, 10464−10472.

(49) Hou, J.; Liu, Z.; Zhang, P. A New Method for Fabrication of Graphene/Polyaniline Nanocomplex Modified Microbial Fuel Cell Anodes. *J. Power Sources* **2013**, *224*, 139−144.

(50) Qiao, Y.; Bao, S.-J.; Li, C. M.; Cui, X.-Q.; Lu, Z.-S.; Guo, J. Nanostructured Polyaniline/Titanium Dioxide Composite Anode for Microbial Fuel Cells. *ACS Nano* **2008**, *2*, 113−119.

(51) Myers, C. R.; Nealson, K. H. Respiration-Linked Proton Translocation Coupled to Anaerobic Reduction of Manganese (IV) and Iron (III) in *Shewanella putrefaciens* MR-1. *J. Bacteriol.* **1990**, *172*, 6232−6238.

(52) Lovley, D. R.; Holmes, D. E.; Nevin, K. P. Dissimilatory Fe(III) and Mn(IV) reduction. *Adv. Microb. Physiol.* **2004**, *49*, 219−286.